Faculty of Medicine
University Of Crete

Structural evaluation of animal ocular models by means of Photoacoustic Microscopy

Stella Avtzi

November 2016

Τμήμα Ιατρικής
Πανεπιστήμιο Κρήτης

Εκτίμηση της δομής μοντέλων ζωικών οφθαλμών μέσω οπτοακουστικής μικροσκοπίας

Στέλλα Αβτζή

Νοέμβριος 2016

- This thesis is completed under the scientific supervision of:

    - Dr. George J. Tserevelakis
    - Prof. Miltiadis Tsilimbaris
    - Dr. Giannis Zacharakis

- The examination committee consists by:

    - Prof. Miltiadis Tsilimbaris
    - Prof. Dimitris Papazoglou
    - Dr. Vangelis Sakkalis

Table of Contents

A. Abstract

Photoacoustic imaging is a rapidly developing new biomedical imaging modality. The previous years photoacoustic imaging has been used to measure brain metabolism[1], for microvasculature and lymph nodes imaging[2], for melanoma detection[3], breast cancer[4], to measure oxygenation[5] etc. Unlike existing ophthalmic imaging technologies photoacoustic imaging combines the capabilities of optical excitation and acoustic detection. Light absorbing biomolecules such as melanin and hemoglobin can provide intrinsic imaging contrast at high sensitivity. In this work, the feasibility of hybrid photoacoustic and optical imaging of two major molecular contrast agents, melanin and lipofuscin, in ocular models was investigated. Imaging was based on two physical processes depending on photon absorption: opto(photo)acoustic effect and autofluorescence. The aim of this work was to obtain structural and molecular information of the ciliary body of healthy rabbit eyes. A series of experiments were performed including the imaging ranging from small parts to whole uncut ciliary bodies. photooacoustic signal was primarily generated due to the absorption of melanin that lies on the RPE cells of the ciliary body, while autofluorescence was mainly emitted by lipofuscin depositions. As a result, this thesis is an effort to test the capabilities of a prototype hybrid microscopy system as to the high resolution label-free imaging of ocular models, constituting a stepping stone for further application potential investigation in opthalmological research.

Α. Περίληψη

Η οπτοακουστική απεικόνιση είναι μια ραγδαία αναπτυσσόμενη τεχνική βιοϊατρικής απεικόνισης. Σε αντίθεση με τις ήδη υπάρχουσες τεχνολογίες, η οπτοακουστική απεικόνιση καταφέρνει να συνδυάσει την οπτική διέγερση με την ακουστική ανίχνευση. Βιομόρια ικανά να απορροφήσουν το φως, όπως η μελανίνη και η αιμοσφαιρίνη, παρέχουν ενδογενή αντίθεση κατά την απεικόνιση με υψηλή ευαισθησία. Στη παρούσα εργασία μελετήθηκε η δυνατότητα υβριδικής οπτοακουστικής και οπτικής απεικόνισης δυο βασικών μοριακών σκιαγραφικών του οφθαλμού, της μελανίνης και της λιποφουσκίνης. Η απεικόνισή τους στηρίχθηκε σε δύο φυσικά φαινόμενα τα οποία βασίζονται στην οπτική απορρόφηση: στο οπτοακουστικό φαινόμενο και στον αυτοφθορισμό. Στόχος αυτής της εργασίας ήταν η απόκτηση δομικής και μοριακής πληροφορίας του ακτινωτού σώματος οφθαλμών υγιών κουνελιών. Έτσι ολοκληρώθηκε μια σειρά πειραμάτων τα οποία περιλαμβάνουν την απεικόνιση μικρών τμημάτων ή και ολόκληρων ακτινωτών σωματων. Το οπτοακουστικό σήμα στηρίχθηκε την απορρόφηση της μελανίνης η οποία βρίσκεται στα μελανοκύτταρα του μελάχρουν επιθηλίου του ακτινωτού σώματος ενώ η απόκτηση εικόνων αυτοφθορισμού ήταν εφικτή λόγω των μορίων λιποφουσκίνης στα ίδια κύτταρα. Συνοψίζοντας, αυτή η πτυχιακή εργασία αποτελεί μια προσπάθεια ελέγχου των δυνατοτήτων του υβριδικού συστήματος μικροσκοπίας ως προς την υψηλή διακριτική ικανότητα μέσω ενδογενούς απεικόνισης οφθαλμικών μοντέλων, αποτελώντας ένα εφαλτήριο για την περεταίτρω διερεύνηση εφαρμογών της οπτοακουστικής απεικόνισης στην οφθαλμολογία.

B. Introduction

Research into the nature of photoacoustic (PA) phenomenon has a long history dating back to 1880 when Alexander Graham Bell first discovered the effect following his observation on the generation of sound due to the absorption of sunlight. During the next years, relatively little scientific research or technological development took place until the development of pulsed lasers providing the necessary high peak power, spectral purity and directionality that PA imaging applications require. This is the reason why it took more than a hundred years following the initial observation of Bell until the phenomenon was exploited in biomedical imaging. In 2003, the first in vivo photoacoustic images were obtained by Wang et al.[6], and a rapid growth began in the field of instrumentation development, image reconstruction algorithms, functional and molecular imaging capabilities and the application of the technique in clinical medicine and basic biological research[7,8].

In photoacoustic imaging, ultrasound waves are excited by irradiating tissue with intensity modulated electromagnetic radiation, usually pulsed on a nanosecond timescale. In PA imaging, optical wavelengths ranging from near-ultraviolet and near-infrared (NIR) spectral regions are most commonly used. The NIR spectral range 600 – 900 nm offers the greatest penetration depth which can extend up to several centimeters. In the case of optical excitation, the light absorption by specific tissue chromophores such as hemoglobin, melanin, water or lipids followed by rapid conversion to heat, produces a small temperature rise (in the order of 0.1 K) below the threshold required to cause physical damage or physiological changes to tissue. This leads to an initial pressure rise, which subsequently relaxes resulting in the emission of broadband acoustic waves at typical frequencies ranging from a few to several tens of MHz. These acoustic waves are usually detected by a single element or an array of piezoelectric ultrasound transducers. Then by measuring the time of arrival for the acoustic waves, an image can be reconstructed either using a back-projection algorithm (tomography) or by employing a direct Hilbert transformation of the signal (microscopy).

In principle, PA imaging is based on the initial pressure distribution produced by the deposition of the optical energy, therefore it depends significantly on the absorption

and scattering properties of the medium. PA imaging provides a great advantage of contrast selectivity, since different chromophores in tissue absorb in specific wavelengths, different molecules can be discriminated by selecting a laser excitation wavelength close to the chromophore absorption peak. However, since excitation is generated by optical methods, the border of penetration depth, due to high tissue scattering, is still valid. Therefore, in PA it is possible to overcome the potentials of classic microscopy going deeper than 1mm in tissue but it is still more limited than ultrasound techniques.

As it has already been mentioned, one of the most prominent absorbers in unstained tissue is melanin. Melanin exists in high concentration in the eye, thus ocular models are excellent candidates for exploring PA imaging capabilities. The last years, PA imaging tends to be combined with classic ophthalmology techniques. Well-established imaging instruments include optical coherence tomography (OCT)[9], fluorescein angiography (FA), color fundus photography and autofluorescence etc. [5,10]. In clinical applications, OCT is often used to generate an anatomical image of the eye, however it cannot provide physiological or functional information.

Several previous studies have attempted to combine photoacoustic with fluorescence imaging or other ophthalmoscopic techniques in order to visualize the anterior or the posterior segment of the eye. For example, optical resolution photoacoustic microscopy (OR-PAM) has been used to image the peripheral ciliary processes, the major iris circle, radial iris arteries, with high spatial resolution down to a few micrometers[5,11]. Furthermore, the ciliary body has also been imaged in detail with adaptive optics photoacoustic microscopy[12].

Jiang et al. [12] has additionally used a system that combines photoacoustic microscopy (PAM) with optical coherence tomography (OCT), called photoacoustic ophthalmoscopy (POAM)[13]. POAM was also integrated with autofluorescence (AF) and were used, to image the posterior segment in eyes of albino and pigmented rats revealing the RPE cells of the retina and the choroidal vessels [14] with lateral resolution of 2.5μm and axial resolution up to 23μm.

This thesis is focused on the application of a hybrid imaging system that combines in a single instrument the advantages of photoacoustic and fluorescence microscopy

modalities regarding ocular imaging. The advantages that this research appears, and discriminates among others is firstly the fact that the acquisition of high resolution images can be obtained, with lateral resolution of 2μm and axial resolution of 30μm. Secondly, although this is still a microscopic technique, a great field of view can be achieved, and finally that it is feasible to acquire three-dimensional information by 2D raster scanning.

In conclusion, we have achieved to image ex vivo the anterior segment of rabbit eyes and more specifically the ciliary body, characterized by high melanin depositions, employing a hybrid imaging system of OR-PAM and fluorescence microscopy. As a result, structural images of the ciliary body are shown or parts of it. Moreover, the advantage of fluorescence microscopy gives us additional information about the retinal pigmented epithelium cells (RPE) that lie in the ciliary body as well. Therefore, we are able to visualize *ex vivo* parts of the eye that traditional ophthalmoscopic techniques cannot, giving us the possibility to adapt this in living animals also.

C. Theory

I. The Photoacoustic Effect

The photoacoustic (PA) effect can be qualitatively described as a five-step process:

- initially an object absorbs electromagnetic radiation energy,
- the absorbed energy is partially converted into heat,
- the temperature of the object increases [15],
- a thermoelastic expansion occurs,
- and acoustic pressure in the medium is generated.

In order to describe mathematically the photoacoustic signal generation arising from pulsed laser sources, we usually make the so-called thermal confinement approximation. According to this assumption, the pulse width is much shorter than the characteristic time of thermal relaxation, therefore no heat is dissipated during excitation. Under these circumstances, the photoacoustic pressure generated in an acoustically homogeneous and non-viscous medium is described by

$$\nabla^2 \mathrm{p(r,t)} - \frac{1}{v_s^2}\frac{\partial^2}{\partial t^2} p(r,t) = -\frac{\beta}{C_p}\frac{\partial}{\partial t} H(r,t) \qquad (1)$$

where $H(r,t)$ is a heating function defined as the thermal energy converted in a spatial position r and time *t* by the electromagnetic radiation per unit volume per unit time, C_p is the isobaric specific heat in $J/(K \cdot kg)$, β is the isobaric volume expansion coefficient in K^{-1}, v_s is the acoustic speed. For practical calculations, the amount of the generated heat by tissue is proportional to the strength of the radiation:

$$H(r,t) = \mu_\alpha(r)\Phi(r,t) \qquad (2)$$

where μ_α is the absorption coefficient and Φ is the optical radiation fluence [16,17] .

The source term of Eq. (1) is proportional to the first time derivative of the heating function, implying thus that the thermoelastic expansion of the medium will give rise to photoacoustic wave propagation only when the heating through the absorption of the

incident irradiation changes over time – a constant light intensity would not cause any photoacoustic effect. This explains the reason why pulsed or intensity-modulated lasers resulting in time-variant heating are exclusively employed for this purpose.

II. Light interactions in tissue

It is essential to briefly describe how the EM radiation field reaches the PA source during its propagation through tissue. In this chapter, the interaction of light with matter and how this introduces scattering, absorption and emission will be also considered. In order to model light propagation, three main concepts will be introduced; light emitters (light sources), light absorbers (or light 'sinks'), and light scatterers. The term light emitters will be referring to all different mechanisms and processes generating visible light in nature, while light "sinks" will absorb part of that visible light. In some cases this absorbed energy will be re-emitted in the form of visible light, as in the case of fluorescence. Typical endogenous tissue chromophores (optical absorbers) include hemoglobin, melanin, and water [17].

In photoacoustic imaging penetration depth is limited ultimately by optical and acoustic attenuations. In general, for most soft tissues, although acoustic attenuation is significant, it is optical attenuation that dominates. Optical attenuation depends on both the absorption and scattering coefficients and is strongly wavelength-dependent.

In optically scattering media such as tissues, optical penetration depth is best characterized by the effective attenuation coefficient μ_{eff} derived from diffusion theory where

$$\mu_{eff} = \sqrt{3\mu_a(\mu_a + \mu_s')} \quad (3)$$

and μ_a and μ_s' are the absorption and reduced scattering coefficients, respectively.

The mean free path or scattering mean free path (MFP) can be defined as:

$$l_s = \frac{1}{\mu_s} \quad (cm) \quad (4)^{18}$$

which describes the mean distance that a photon travels between two scattering events. In case where the anisotropy of the medium is taken into account, the reduced scattering coefficient can be defined as:

$$\mu'_s = \mu_s(1-g),\ \ (cm^{-1}) \quad (5)$$

In the above equation *g* is the anisotropy function defining the degree of forward scattering, expressed as a probability function by a Henyey-Greenstein phase function with a coefficient, *g*. For photon scattering in tissue, *g* is typically 0.8–1.

Using the reduced scattering coefficient, the transport mean free path (TMFP) can then be defined as:

$$l_{tr} = \frac{1}{\mu'_s} \quad (6)$$

The TMFP describes the distance that light has to travel until its propagation is completely randomized (diffused). Combining equations (4), (6) it comes up that $l_s = l_{tr}(1-g)$. The higher the *g*, the more forward the scattering and the longer it takes for light to become diffuse, resulting in higher penetration distances through samples

In homogeneous scattering media, once at a depth beyond several transport mean free paths (approx. 1 mm), the light becomes diffuse and the irradiance decays exponentially with depth.

In Figure 1 the so-called “optical window” is shown, which describes the section in the near infrared spectra, where most of the main tissue absorbers (hemoglobin, water, melanin) have the least possible absorption.

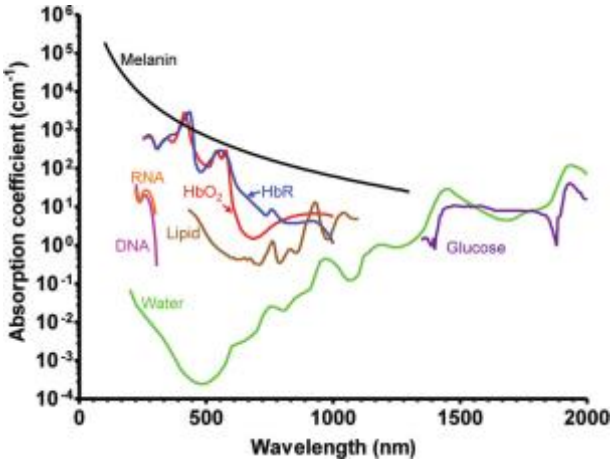

FIGURE 1: THE OPTICAL WINDOW IN THE OPTICAL AND NEAR INFRARED REGION WHERE THE MAIN ABSORBERS IN TISSUE HAVE THE LEAST POSSIBLE ABSORPTION, ALLOWING THUS LIGHT TO PENETRATE.

Although μ_a is much smaller than μ_s' in scattering tissue, the wavelength dependence of μ_s' is significantly smoother compared to that of μ_a over the visible and NIR spectral region. Thus, the scattering by the tissue plays an important role for the variations in the illumination depth, and consequently the detection depth of PA detection.

However, imaging contrast can be assumed to be dominated by the optical absorption and scattering properties of the tissue. In fact, optical absorption tends to dominate and for this reason PA images are often described as being 'absorption based'. However, it is important to recognize that this does not mean that imaging contrast is directly proportional to the absorption coefficient μ_a .

The dominance of optical absorption as the primary source of PA image contrast enables PA imaging as to the visualization of anatomical features that contain an abundance of chromophores such as hemoglobin, lipids and water.

III. Fluorescence

Fluorescence imaging can be considered as a complementary modality to photoacoustic imaging in the same experimental setup. In general, absorption is the process during which light photons transfer their energy to an atom or molecule. The process takes place by promoting an electron from an orbital in the ground state to an unoccupied orbital in an excited state with an energy difference equal to the energy of the photon. In room temperature, it can be assumed that most electrons in the molecule are in their ground state.

Depending on the energy absorbed and the quantum selection rules, several transitions can be permitted from the ground state to the first, second or higher excited states. Once the electron is at an excited state, there are several paths that can be followed in order to return to the ground state, and therefore to the state of minimum energy. After absorption of a photon, the system can follow a number of different paths; it can either lose energy via vibrational relaxation reaching the lower vibrational level of the specific excited state or undergo intersystem crossing towards a triplet electronic state. From a singlet excited state a photon can relax by radiative emission

(fluorescence) to the ground state and similarly from the triplet state it can relax radiatively via phosphorescence (will not be discussed here). The radiated photon has lower energy than the excitation photon due to the vibrational relaxation and subsequent loss of energy which corresponds to a shift in the emission wavelength to higher values, the so called ‘Stokes shift’.

IV. Photoacoustic Microscopy (PAM)

In general, the great advantage of classical optical microscopes relies on the sharp optical focusing. Though, as mentioned previously this advantage is quickly lost as photons travel deep into tissue, which is a highly scattering medium in the optical range, therefore when photons reach the optical diffusion limit (approximately 1mm in tissue) several scattering events have occurred and light focusing is impossible due to random photon paths.

In contradiction to photoacoustic tomography (PAT) of larger samples, PAM is mainly used for high resolution imaging up to few μm of small areas. Some significant properties of PAM over PAT are: the tight focusing with subsequent improved image resolution, the fact that point by point scan is feasible and that the reconstruction algorithm is not based on back projection algorithm.

Photoacoustic Microscopy (PAM) can be classified into two categories depending on the type of focusing.

- Optical Resolution PAM (OR-PAM): where the optical focusing is tighter than the acoustic focusing
- Acoustic Resolution PAM (AR-PAM): where the acoustic focusing is tighter than the optical

However, the detection sensitivity can be maximized when the optical illumination and the acoustic detection are confocally aligned. AR- or OR- PAM are individually used depending on the depth of imaging. OR-PAM has a great advantage over AR-PAM in spatial resolution since the optical beam can be focused in a much tighter spot than

the acoustic due to the fact that optical wavelengths are shorter than the acoustic. Though, the disadvantage is that OR-PAM is limited within the optical diffusion limit due to light scattering. This is where AR-PAM dominates over OR-PAM since it takes advantage of weaker acoustic scattering and achieves better focusing. Typical examples of each modality setup are presented at Figure 2.

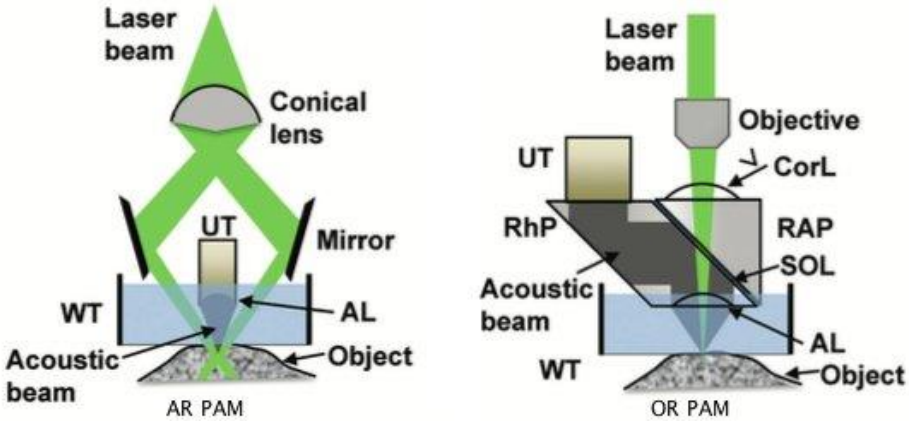

FIGURE 2: TYPICAL SETUP EXAMPLES OF OR AND AR PAM

In general, the axial resolution in PAM is determined by the imaging depth and the frequency response of the transducer, the lateral resolution is determined by the point spread function of the dual focal points[19].Typical values of OR- and AR- PAM lateral resolutions are approximately 2μm and 20μm respectively. Although the axial resolution depends on the central frequency of the transducer, typical resolution value for PAM in general 10μm.

Lateral Resolution

The lateral resolution of OR-PAM $R_{L,OR}$ depends on the diffraction limit spot size of the optical focus:

$$R_{L,OR} = 0.51 \frac{\lambda_o}{NA_o} \quad (7)$$

where λ_o is the wavelength and NA_o is the numerical aperture of the optical objective. The constant 0.51 derives from the FWHM of the focal spot in light intensity.

In AR-PAM the light beam is weakly focused into the tissue. As a result, the light beam diameter is larger than the acoustic focus. In this case the lateral resolution of AR-PAM is given by:

$$R_{L,AR} = 0.71\,\frac{\lambda_A}{NA_A} = 0.71\,\frac{v_A}{NA_A \cdot f_A}$$

where NA_A is the numerical aperture of the ultrasonic transducer, v_A is the speed of sound in the medium and λ_A , f_A are the central wavelength and the central frequency of the photoacoustic signal.

Axial Resolution

For axial resolution both techniques share the same formula (Eq.9) based on two assumptions. Firstly, to the assumption that the PA response to a point target follows a Gaussian frequency profile. Secondly, assuming that the PA signal bandwidth is larger than the transducer detection bandwidth and it is proportional to the central frequency f_A.

$$R_{A,OR/AR} = 0.88\,\frac{v_A}{\Delta f_A} \quad (9)$$

where Δf_A is the PA signal bandwidth.

V. The Anatomy of the Eye

The wall of the eye has three layers: the fibrous tunic, the vascular tunic and the neural tunic [20].

Fibrous tunic

The fibrous tunic is the outermost layer of the eye and consists of the sclera and the cornea. Most of the ocular surface is covered by the sclera (the ‘white’ of the eye), which is made up of dense fibrous connective tissue containing collagen and elastic fibres. The surface of the sclera contains small blood vessels and nerves. The

transparent cornea is continuous with the sclera and is made up of a dense matrix of fibres laid down in such a way that they do not interfere with the passage of light.

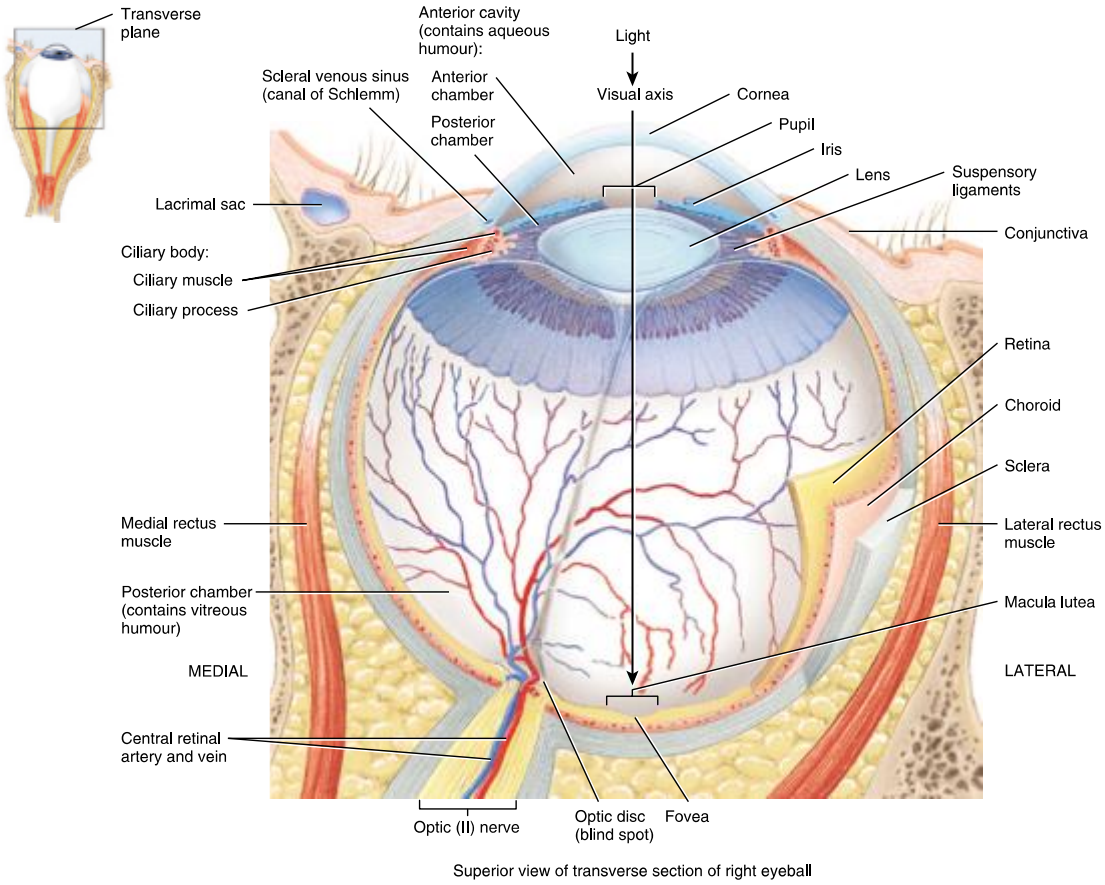

FIGURE 3: ANATOMY OF THE EYE

Vascular tunic

The vascular tunic is the middle of the three layers of the eye and contains numerous blood vessels, lymph vessels and the smooth muscles involved in eye functioning

The vascular tunic is made up of:

- the iris
- the ciliary body
- the choroid.

Iris

The iris is the central, colored portion of the eye and regulates the amount of light entering the eye by adjusting the size of the central opening (the pupil). It is formed of two layers of pigmented cells and fibres and two layers of smooth muscle (the pupillary muscles):

- pupillary constrictor muscles
- pupillary dilator muscles.

Both sets of muscles are controlled by the autonomic nervous system; activation of the parasympathetic nervous system leads to constriction of the pupil in response to bright light. Activation of the sympathetic nervous system leads to the dilation of the pupil in response to dim light levels. At its edge the iris attaches to the anterior part of the ciliary body.

Ciliary body

The greatest part of the ciliary body is made up of the ciliary muscle, a smooth muscular ring that projects into the interior of the eye. The epithelial covering of this muscle has many folds called ciliary processes. The suspensory ligaments of the lens attach to the tips of these processes. Though since the ciliary body is the main area of the eye studied in this thesis, further details will be discussed below.

Choroid

The choroid is a vascular layer that separates the fibrous and neural tunics. It is covered by the sclera and attached to the outermost layer of the retina. The choroid contains an extensive capillary network that delivers oxygen and nutrients to the retina.

Neural tunic (retina)

This is the innermost layer of the eye, consisting of a thin outer layer called the pigmented part and a thicker inner layer called the neural part.

- The pigmented part of the retina absorbs the light that passes through the neural part; this

- prevents light bouncing back through the neural part and causing ‘visual echoes’.

The neural part of the retina contains light receptors, support cells and is responsible or the preliminary processing and integration of visual information. These receptor cells are the cells that detect light (photoreceptors).

- Rods
  These photoreceptors do not discriminate between colors. They are very sensitive and enable us to see in very low light levels. Rods are mostly concentrated in a band around the periphery of the retina, and this density reduces towards the center of the eye.

- Cones
  These photoreceptors provide color vision and give sharper, clearer images than the rods do, but they require more intense light. Cones are mostly situated in the macula lutea and particularly at its center in an area called fovea. The elongated outer sections of the rods and cones contain hundreds to thousands of flattened membranous discs. In the rods the discs are separate and form the shape of the cylinder.

There are three types of cones (red, blue and green), and colour discrimination is based on the integration of information received from the three types of cones. For

instance, yellow is shown by highly stimulated green cones, less strongly stimulated red cones and a relative lack of stimulation of the blue cones.

A narrow connecting stalk links the outer segment to the inner segment, which is the part of the cell that contains all the usual cellular organelles. The inner segment is also the area where synapses with other cells are made and neurotransmitters are released.

The rods and cones synapse with neurons called bipolar cells, which in turn synapse within a layer of neurons called ganglion cells. At both these synapse areas there are associated cells that can stimulate or inhibit the communication between the two cells, and therefore alter the sensitivity of the retina (for instance, in response to very bright, or dim, light levels).

Axons from approximately 1 million ganglion cells converge on the optic disc, at which point they turn and penetrate the wall of the eye and proceed to the diencephalon of the brain as the optic nerve. The central retinal artery and vein pass through the centre of the optic nerve. The optic disc contains no photoreceptors, and thus this area is known as the blind spot; however, we do not notice the blind spot in our vision as involuntary eye movements keep the visual image moving and the brain can thus supply the missing information.

The Ciliary body

The ciliary body is a ring of tissue on the inner wall of the eyeball, positioned just behind the rear- facing (posterior) surface of the iris [21]. The base of the ciliary body is home to the ciliary muscle, the contraction of which causes the lens to assume a more rounded shape. This is because the lens is suspended by fine ligaments, called zonules that attach to the ciliary body. When the ciliary muscle contracts, the anchoring point of the zonules moves slightly inward, relaxing tension on the zonules, and the natural elasticity of the lens causes it to take on a more spherical shape. This is called the process of accommodation. When the ciliary muscle relaxes, there is a slight outward motion that tightens the zonules and flattens the lens. A typical image of the ciliary body is shown in the schematic representation below (Figure 4).

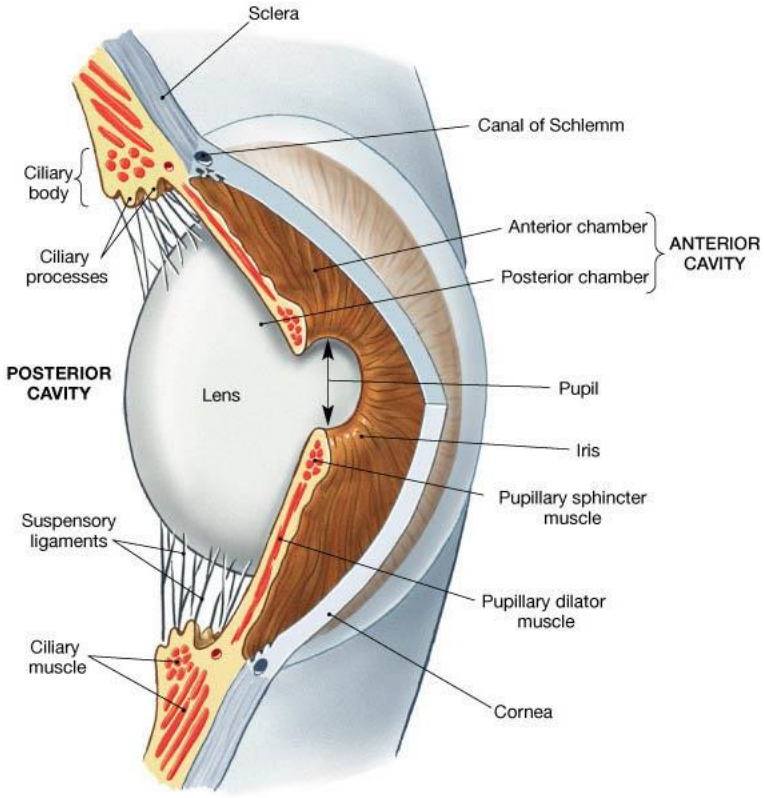

FIGURE 4: DETAILED IMAGE OF THE POSITION AND THE BASIC FUNCTION OF THE CILIARY BODY THAT IS THE ABILITY TO HOLD THE CRYSTALLINE LENS THROUGH THE ZONULAR FIBRES AND HELP WITH THE ACCOMODATION

Function

The ciliary body has two principal functions:

1. It produces and secretes aqueous humour that is essential to regulate the pressure within the eye.
2. It contains muscles that act on the crystalline lens via its zonular fibres, in concert with the elastic lens capsule, to change its shape and thus shift the focus of the eye from far to near.

Structure

The surface of the ciliary body is elaborated into a series of ridges named ciliary processes. On the ciliary body, the purpose is to increase the surface area available for fluid secretion. The ciliary processes have a radial orientation, each ridge pointing toward the pupil as shown in Figure 5.

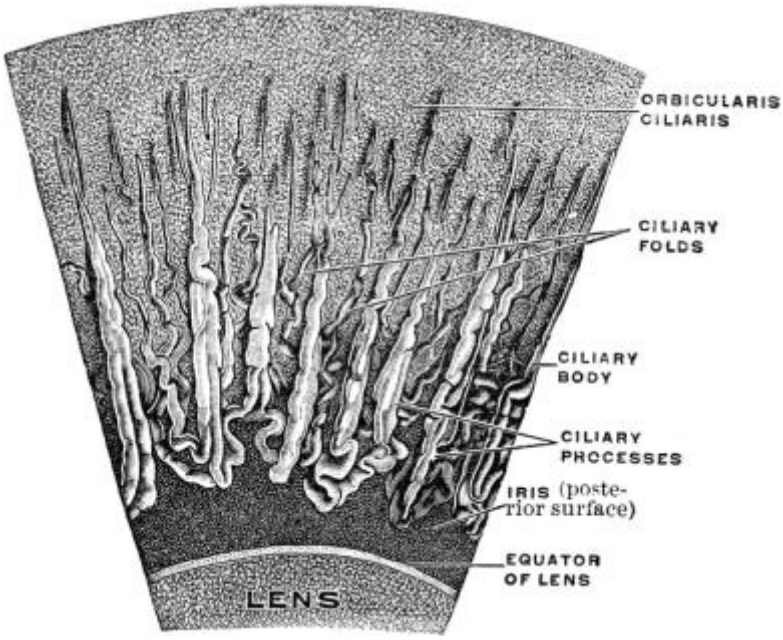

FIGURE 5: PART OF THE CILIARY BODY IS PRESENTED.

The entire surface of the ciliary body, the ridges as well as the valleys in between, is covered with a ciliary epithelium. In the ciliary epithelium bilayer, the two cell layers have different developmental origins. The cell layer farthest from the interior of the eyeball is developmentally related to the retinal pigment epithelium. True to their origin, these cells contain black pigment granules, and not very creatively, this half of the ciliary epithelium bilayer has been termed the pigmented cell layer. The other half of the bilayer, the non-pigmented layer, is developmentally related to the neural retina. The pigmented and non-pigmented ciliary epithelial cells (PE and NPE) have numerous differences other than the presence or absence of pigment.

D. Materials and Methods

I. Experimental Setup

The system is consisted of a modified inverted microscope incorporating photoacoustic and fluorescence imaging modalities. A 3D representation of the hybrid microscopy system is presented in Figure 6, demonstrating the basic setup components.

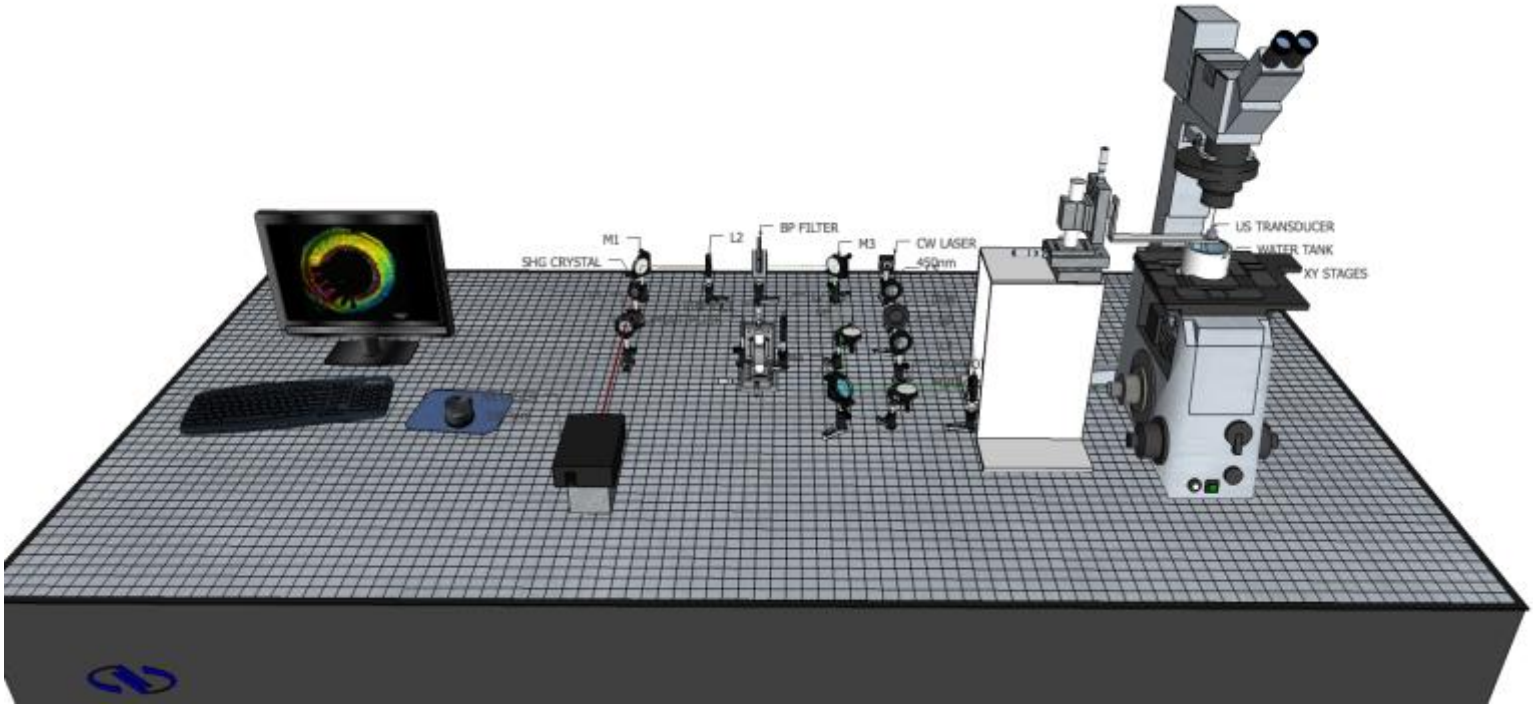

FIGURE 6 : 3D REPRESENTATION OF THE EXPERIMENTAL SETUP

A more detailed schematic representation of the setup is shown in Figure 7.

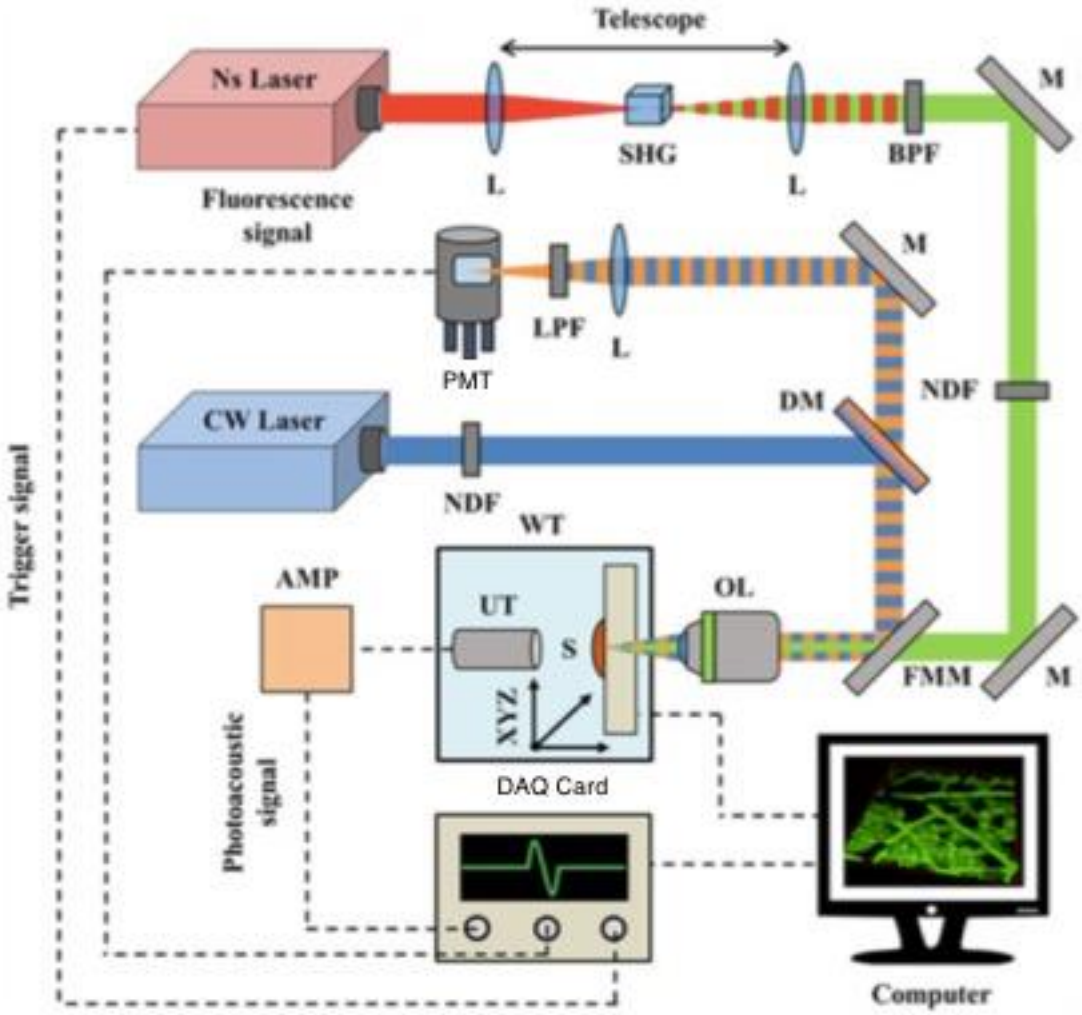

FIGURE 7 : SCHEME OF THE HYBRID IMAGING SYSTEM. L, LENS; M, MIRROR; SHG, SECOND HARMONIC GENERATION CRYSTAL; BPF, BAND-PASS FILTER; LPF, LONG-PASS FILTER; NDF, NEUTRAL DENSITY FILTER; DM, DICHROIC MIRROR; PMT, PHOTOMULIPLIER; FMM, FLIP MOUNT MIRROR; WT, WATER TANK; AMP AMPLIFIER; UT ULTRASONIC TRANSDUCER; DAQ: DATA ACQUISITION CARD ; OL OBJECTIVE LENS; S, SPECIMEN; XYZ, MOTORIZED XY AND MANUAL Z STAGES. [22]

The OR-PAM modality employs a diode pumped nanosecond laser source emitting at 1064nm in IR with 10 ns pulse width and 6.8 kHz repetition rate. The laser beam is focused on a second harmonic generation crystal (SHG) in order to obtain a visible wavelength at 532 nm. This wavelength was specifically selected due to its ability to excite efficiently the basic chromophores in tissue: melanin and hemoglobin. Subsequently, the beam passes through a second lens to form a telescopic configuration which expands the beam approximately two times. A bandpass (BP) filter is further placed to permit only the visible wavelengths to pass from (FWHM: 511-

551 nm). A number of neutral density filters is also placed in order to attenuate the laser beam energy at the focal plane and prevent potential damage of the specimen. Finally, the light beam is guided into the inverted microscope through some highly reflective mirrors.

An objective lens with 0.2 NA is placed to focus the beam tightly onto the specimen. The sample is placed on a microscope glass and then it is fixed at the bottom of an optically clear water tank. The positioning of the sample prior each imaging session, as well as the respective raster scanning during a measurement is performed by two μm resolution XY motorized stages. The focus position on the z-axis is performed manually using the microscope control. In addition, the tank was filled with distilled water in order to provide an efficient acoustic coupling between the photoacoustic sources and the detection unit [22].

At the superior side of the sample an ultrasonic transducer, with central frequency of 20 MHz, is placed in a confocal and coaxial configuration with respect to the illumination focus. The detected ultrasound signals are subsequently amplified using a low noise RF amplifier and recorded through a DAQ card connected to a computer [23]. In addition, the acquisition onset of the time-domain photoacoustic signal was triggered internally by the control unit of the nanosecond laser source. Finally, three-dimensional reconstruction was performed by using a custom made algorithm that calculates the modulus of the Hilbert transformation of the signal [23].

The fluorescence modality of the hybrid setup employs a continuous wave (CW) diode laser emitting at 450nm as an excitation source. The beam is initially attenuated and guided through highly reflective mirrors to a long pass dichroic mirror that reflects wavelengths lower than 505nm and subsequently focused by the same objective lens. The imaging of the area of interest is similarly achieved by mechanical raster scanning of the sample over the beam focus.

The back-scattered fluorescence light is transmitted through the dichroic mirror, passes through a long pass filter and is finally focused on a PMT. The measured signal is recorded using the same DAQ card as in the case of photoacoustic imaging. The system control and the data processing were performed using customized software.

It is also of significant importance to estimate the maximum lateral resolution of the system, which is defined by the diffraction limited laser spot both for the optoacoustic and the optical modality. To calculate the lateral resolution of OR-PAM, we have used Eq. (7) for an 0.2 NA objective and 532nm laser source:

$$R_{L,OR} = 0.51\,\frac{\lambda_o}{NA_o} = 0.51\,\frac{532nm}{0.2} \approx 1.3\mu m$$

Due to the fact that the back aperture of the objective lens is underfilled to achieve a higher depth of field, the effective NA is approximately half of the nominal one, resulting in a maximum lateral resolution of ~3 μm.

The axial resolution of the system is defined by Eq.(8) :

$$R_{L,AR} = 0.71\,\frac{\upsilon_A}{NA_A \cdot f_A} = 0.71\,\frac{1500\,\frac{m}{s}}{0.1\;23MHz} = 46\;\mu m$$

where the average speed of sound 1500 m/s in soft tissue is taken into account.

II. Sample Preparation

To evaluate the imaging capability of the hybrid microscopy system in ocular imaging, eyes of healthy adult rabbits were used as samples. Right after the extraction, two little holes were made in each side of the eye bulb. Afterwards the samples were placed in

clear ethanol and stayed there overnight. The day after, the samples were embedded in glutaraldehyde solution 5% (glutar). Glutaraldehyde is an organic compound, which has the form of an oily colorless liquid and is used as a sterilization agent and preservative. Since the ciliary body lies in the anterior segment, the eyes had to be dissected in the middle. Then, depending of the area of interest the sample was either segmented in more parts or was directly imaged without any further processing.

In order to place the sample in the water tank, the sample had to be fixed on a thin microscope coverslip. For this purpose, agar solution 2% was prepared to serve as a stabilizing medium. Subsequently, the samples were immersed within the agar solution, remaining for a few minutes till stabilized. Afterwards, the glass was placed and fixed at the bottom of the tank, filled with distilled water. Finally, the tank was further fixed on the XY motor stages of the microscope.

The next important step prior a measurement was to find the focal plane on the sample. After obtaining a focused brightfield image of the sample, the sample was moved manually on z-axis at a pre-defined distance towards the objective lens. In this manner, it was ensured that the sample was found along the optical focal zone. Finally, the ultrasonic transducer was placed on a XYZ stage above the sample and was immersed into the distilled water of the tank.

The hybrid imaging system and the microscope stages were controlled by a custom made software in Labview environment. In contrast to several optical microscopy techniques, photoacoustic microscopy can provide 3D reconstructions even though 2D scanning of the sample is performed, due to the measurement of the different times of flight for the generated signals.

III. Image Reconstruction

During each measurement the pressure wave in eiach pixel of the scanned object is recorde. An example of the recorded signal is depicted in Figure 8.

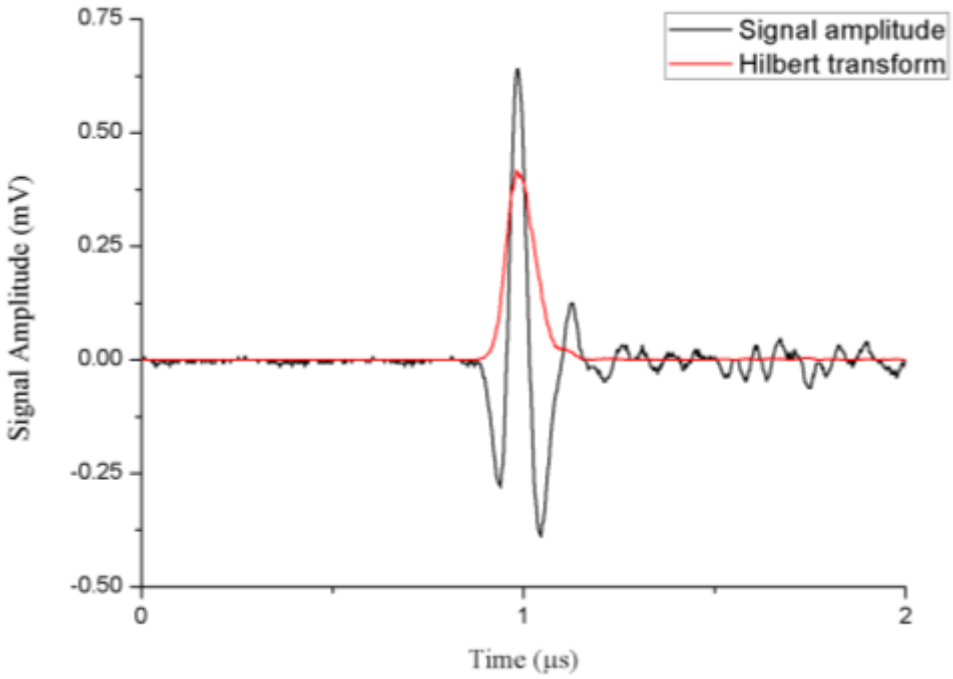

FIGURE 8: EXAMPLE OF THE RAW SIGNAL OBTAINED IN EACH MEASUREMENT

As shown above (Figure 8), black line indicates the recorded acoustic signal amplitude. Raw data obtained from the system are the result of the calculation of maximum amplitude in each scanned point, and these are called the Maximum Amplitude Projection (MAP) images. In addition, red line indicated the Hilbert transformation of the signal that takes into account only positive values, on which the reconstruction algorithm is based on. Furthermore, the full width at half maximum (FWHM) represents the axial bandwidth of the signal.

The position of the maximum intensity signal over time, provides information for different depths providing thus an additional important advantage to photoacoustic imaging. Although 2D scanning is performed during each measurement, by calculating the time of flight of the signal from each plane of the scanned sample till it is recorded to the ultrasonic transducer, 3D information can be reconstructed.

E. Results

In this section of the thesis, we will present the results of a series of experiments on rabbit eyes specimens. The rabbit eyes and more specifically the ciliary body are considered to be ideal samples for hybrid photoacoustic and fluorescence imaging,

due to the high concentration of melanin, as well as the strong autofluorescence signals of lipofuscin depositions respectively.

The first imaging attempt was aiming to the evaluation of the generated signal intensity in small parts of the ciliary body. Figure 9 depicts the maximum amplitude projection (MAP) of four different samples of the ciliary body originating from the same rabbit eye. The first row shows an extended field of view of the imaged sample covering an area in the order of 4000 x 4000 microns. The pixel size for these images is approximately 14 microns.

Afterwards, as shown in the second row of Figure 9, we zoomed in a central area (2000 x 2000 microns) of each sample to resolve finer spatial details (pixel size approx. 7 microns).

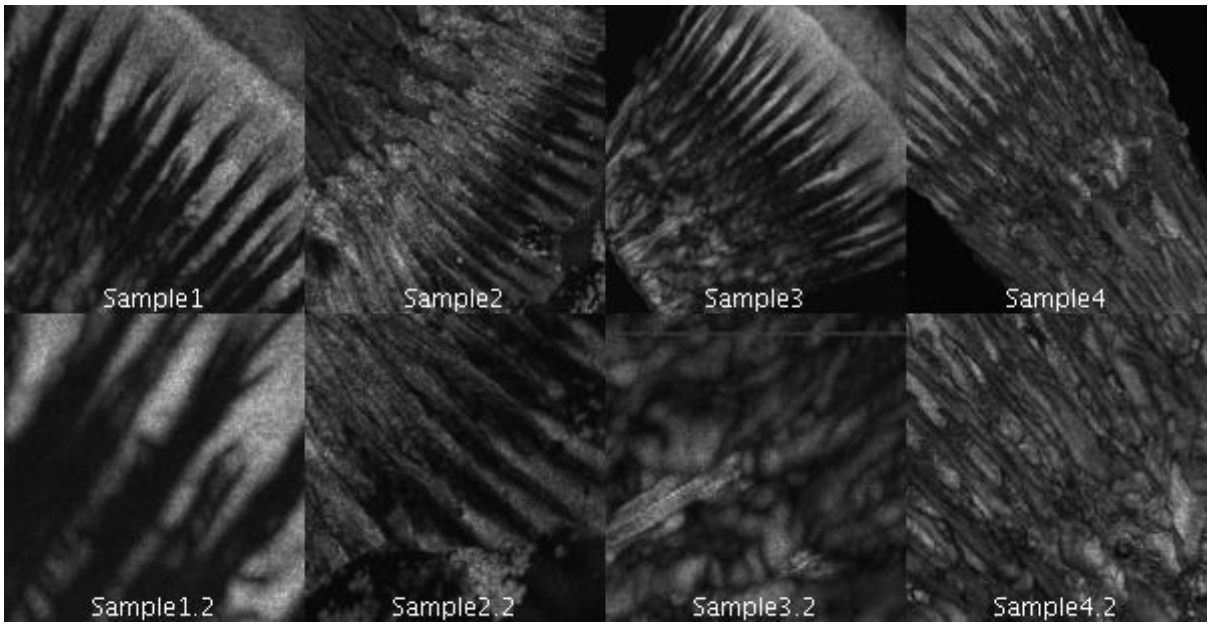

FIGURE 9: MAP IMAGES OF FOUR DIFFERENT SAMPLES FROM THE CILIARY BODY OF THE SAME EYE. THE ABOVE LINE PRESENTS A LARGE VIEW OF EACH SAMPLE, WHERE THE BOTTOM LINE IS A DETAILED ZOOM IN OF EACH

The raw data underwent further processing in order to generate a series of slice images using a custom made algorithm in MATLAB environment. The resulting images were loaded in ImageJ and a depth color code was applied (Figure 10).

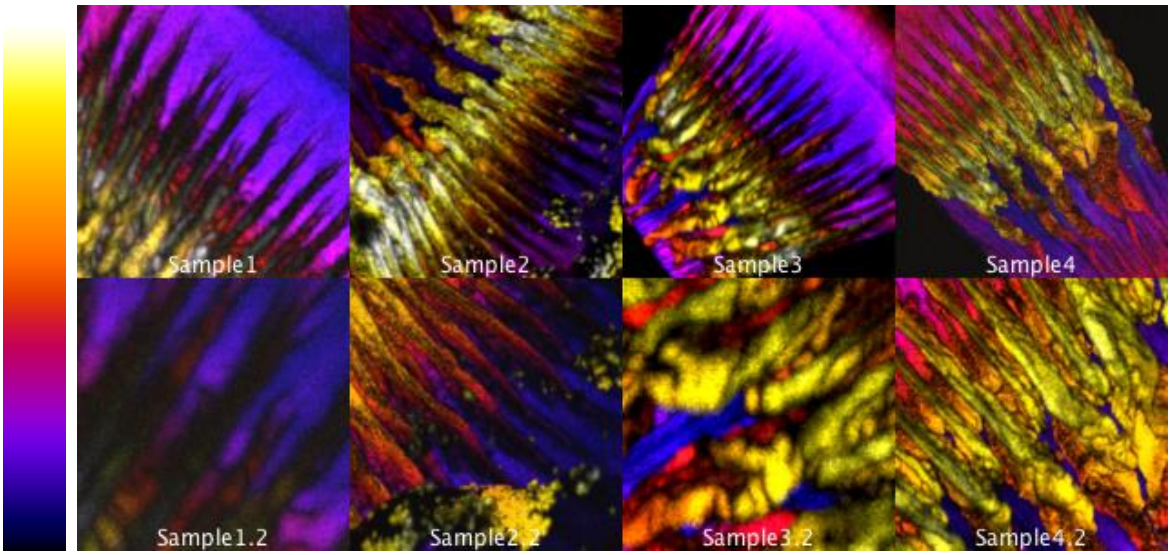

FIGURE 10: RESULTS OF THE FIRST EXPERIMENT WHERE THE RECONSTRUCTED IMAGES OF THE RAW DATA OF FIGURE 9 ARE PRESENTED. THE COLOR BAR ON THE LEFT INDICATES DIFFERENT DEPTH. BLUE COLOR STANDS FOR LOWER DEPTHS.

Different color of the scale bar in the left represents different axial distances, with blue color indicating lower planes, and yellow color showcasing higher planes.

In addition, 3D projections of the same samples are also presented in Figure 11. In these images, it is easy to discriminate parts of the anterior segment of the eye with high melanin deposition. For instance, parts of the iris are distinguished but also the ciliary processes are the ones that dominate.

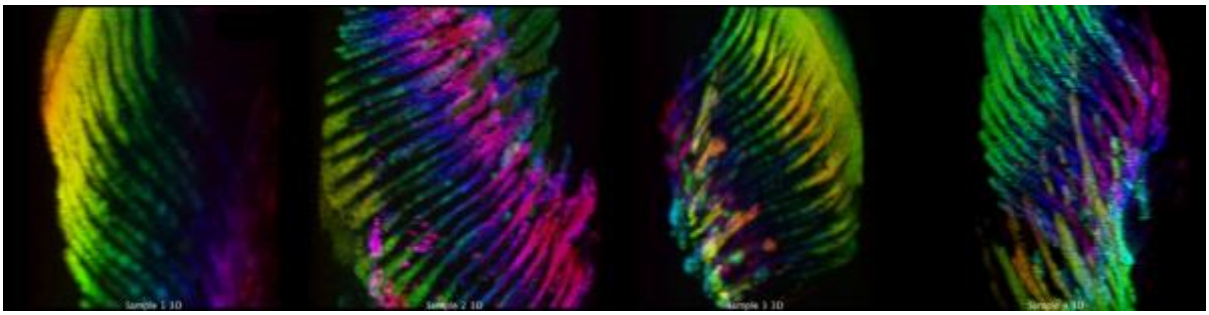

FIGURE 11: 3D IMAGES OF PARTS OF THE CILIARY BODY

Since these first results were obtained, the next experimental step was to verify the capability of the system to obtain a larger field of view with an adequate spatial resolution. For this reason, uncut parts of ciliary bodies were used as specimens. Similarly, for this case, eyes of healthy rabbits were measured and the same procedure was followed as described in section D II. Some typical results of these experiments are presented below.

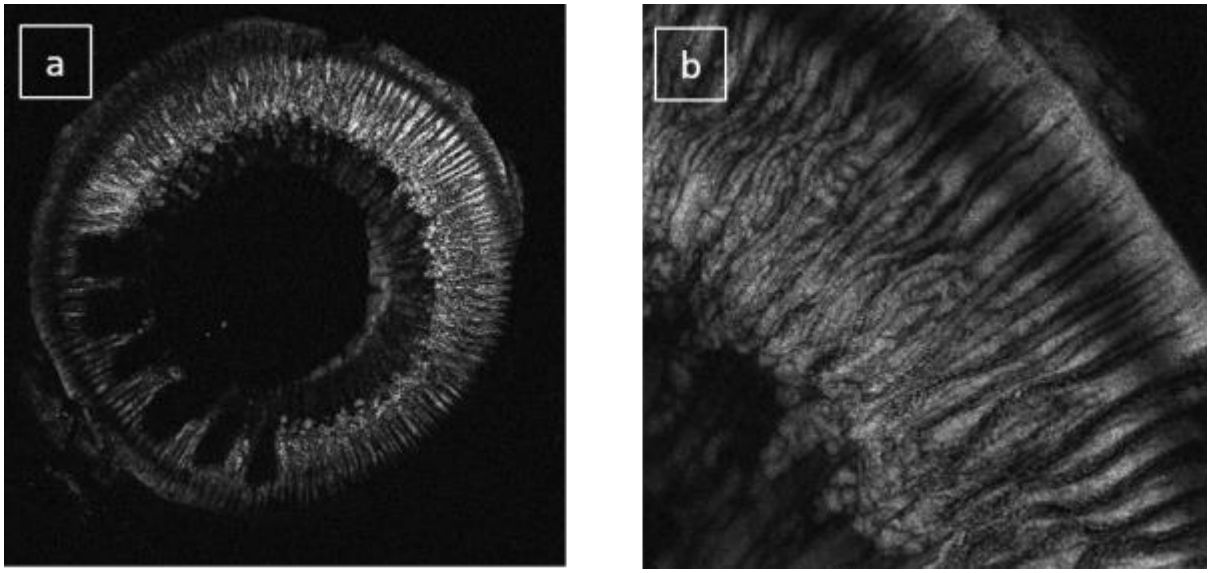

FIGURE 12 : RAW DATA OF THE FIRST UNCUT CILIARY BODY OF A RABBIT EYE. THE IMAGE ON THE LEFT PRESENTS THE WHOLE EYE WHERE THE IMAGE ON THE RIGHT IS A ZOOMED IN SCANNED AREA.

More specifically, Figure 12a depicts an extended 16 x 16 mm field of view region covering the whole eye with a pixel size equal to 40μm. On the other hand, Figure 12b

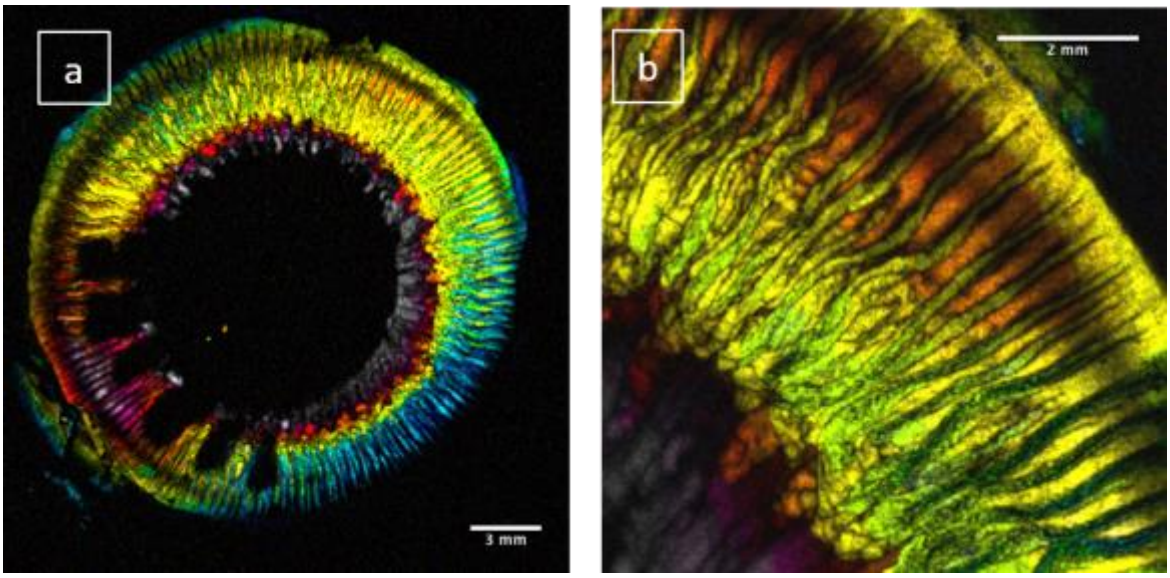

FIGURE 13: RECONSTRUCTED DATA OF AN UNCUT CILIARY BODY. PICTURE 12B PRESENTS A ZOOMED IN AREA OF THE SAMPLE ON THE LEFT. DIFFERENT COLORS INDICATE DIFFERENT SLICE DEPTH

presents a zoomed in area of 4 x 4 mm with significantly lower pixel size, in the order of 13.3 μm.

Similarly, the ciliary processes are easily discriminated, while some discontinuities have appeared in the case of whole eye imaging. A first assumption for such artifacts is that there is some dysplasia present in this eye. Furthermore, Figure 13a and 13b represent the same sample, this time shown with a depth color code in order to reveal more accurately the three dimensional features of the ciliary body.

Continuing in the same spirit as above, an eye of a different rabbit was also examined. In this case, probably due to the filling with agar, the iris was compressed axially, leading to a deformation as it is apparent in Figure 13a and 13b.

The scanning parameters in Figure 14a was 16 x 16 mm with a pixel size of 40 μm, whereas in Figure 14b the area scanned was 4 x 4 mm with a respective pixel size equal to 13.3μm. In the same philosophy, the depth coded reconstructed data is presented in Figure 15.

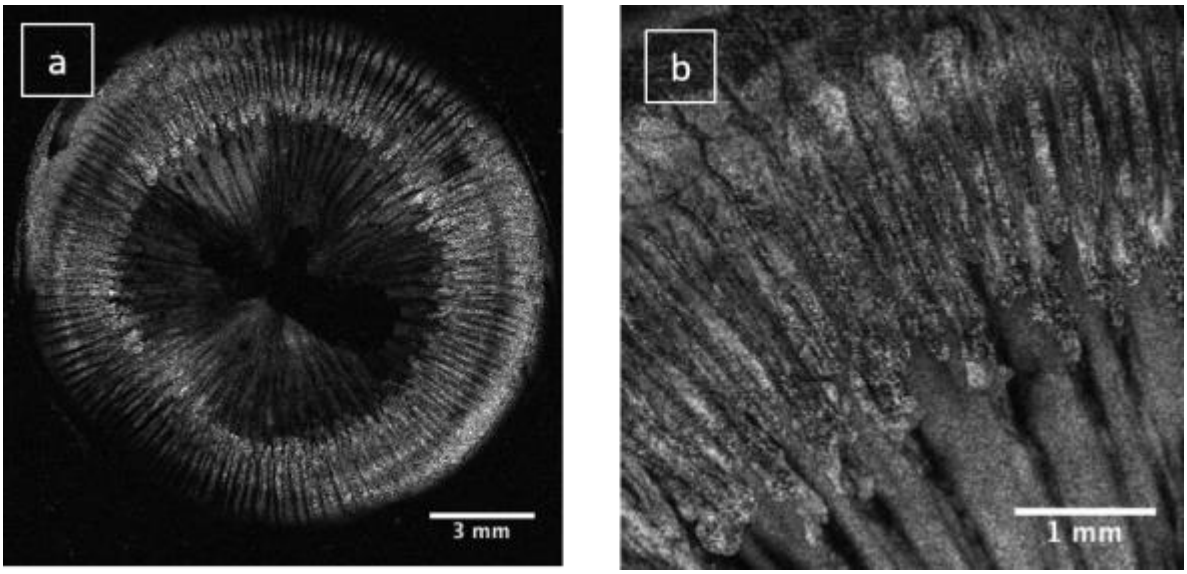

FIGURE 14: RAW DATA OF THE CILIARY BODY OF A SECOND EYE. PICTURE 13A INDICATES THE WHOLE CILIARY BODY WITH A RESOLUTION OF 40 MICRONS WHERE IN PICTURE 13B A ZOOMED IN AREA OF THE SAME SAMPLE IS SHOWN. THE RESOLUTION IS 13.3 MICRONS.

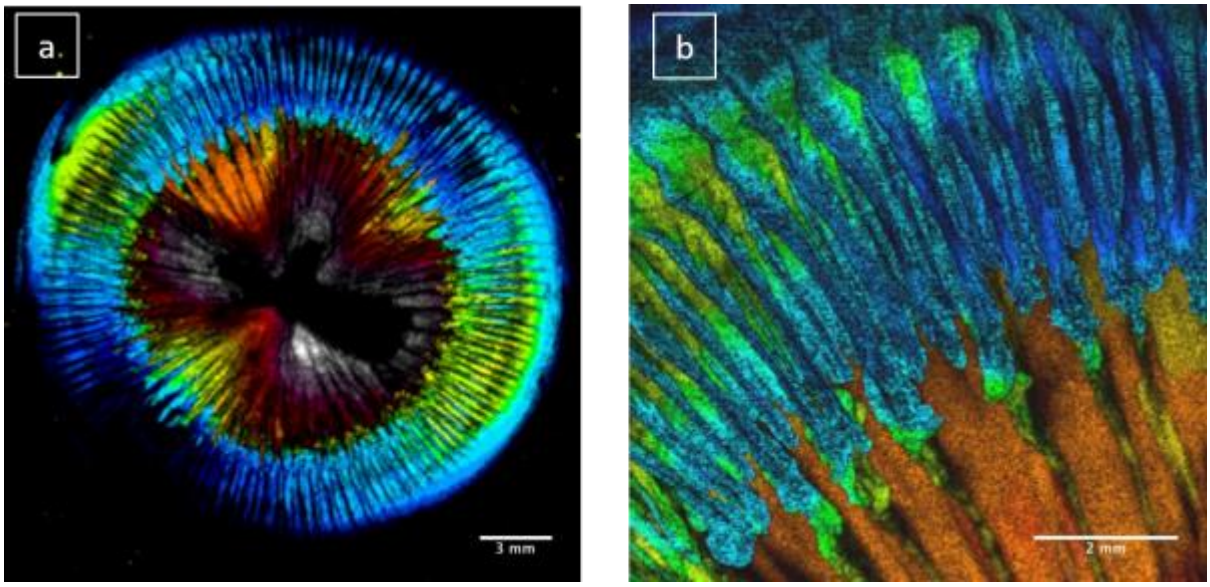

FIGURE 15 : RECONSTRUCTED IMAGES OF THE SAME DATA AS ABOVE. AGAIN DIFFERENT COLORS INDICATE DIFFERENT SLICE DEPTH.

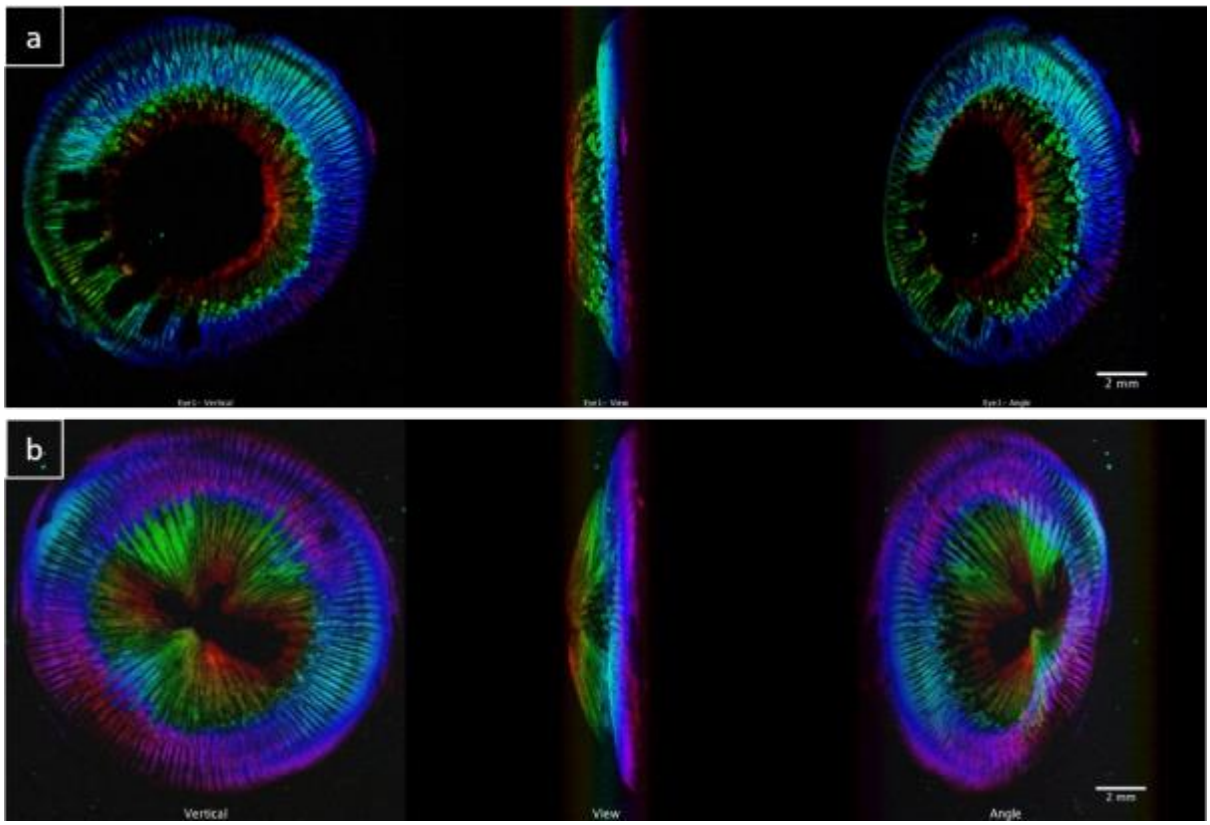

FIGURE16: EACH ROW INDICATES THE TWO EYE SAMPLES. DIFFERENT VIEWS OF THE EACH SAMPLE ARE PRESENTED GIVING THE OPPORTUNITY TO OBSERVER THE WHOLE VOLUME

In Figure 16, different views of the samples described previously in Figures 13a and 15a are presented. By reconstructing the 3D volumes, it is possible to discriminate the most important areas imaged, the iris and the ciliary body.

Following the acquisition of the topography of the ciliary body of the eye via photoacoustic microscopy, the next step tried was to test the maximum obtained spatial resolution of the system by employing a different objective lens. To achieve this, a 0.4 NA objective lens was used in order to increase the lateral resolution of our images when scanning a relatively limited area. A technical difficulty for this case was that by using a higher NA lens the depth of field is much shallower, therefore 3D information is rather limited.

Figure 17c, represents an 80 by 80 μm field of view with 400 nm pixel size, where one can distinguish RPE cells can by their characteristic shape.

Image 17a,b constitutes a comparison of previous published data[12] where RPE cells of a pig eye are shown before and after applying adaptive optics in PAM for improving imaging quality. It is obvious that our recorded data reveal similar structures which are directly comparable to the current literature, verifying in this manner the reliability of our setup.

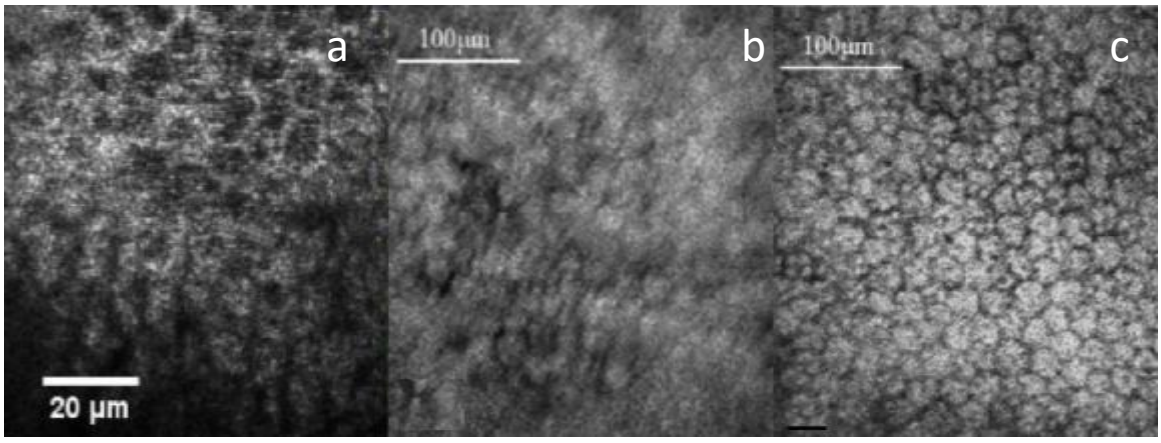

FIGURE 17:A IS AN EXAMPLE OF OUR DATA OBTAINED WITH 0.4 NA LENS SHOWING ALSO RPE CELLS OF THE CILIARY BODY. B,C REPRESENT PREVIOUS PUBLISHED DATA SHOWING RPE CELLS OF A PIG EYE WITHOUT AND WITH APPLYING ADAPTIVE OPTICS IN PAM.

According to the current literature, the main light-absorbing components in RPE at 532 nm are melanin and lipofuscin. Nevertheless, previous works have shown that

lipofuscin does not generate detectable PA signals at the same wavelength. Therefore, it is the melanin distribution both inside and outside the RPE cells that probably provide the necessary signal. From the images it is obvious that the boundaries among the RPE cells have no or weak PA signals, which means that RPE melanin concentrates inside the cells. On the other hand, a weak signal region inside each RPE cell is present. A hypothesis could be that these “dark spots” represent the location of the cell nucleus.

Multimodal Imaging

As already has been mentioned, the imaging system gives the capability of complementary fluorescence imaging. Due to the wide field configuration of the fluorescence modality, only 2D images can be acquired.

It was observed, due to a slight misalignment between the two laser beams, the resulting foci at the focal plane of the sample did not coincide both axially and laterally. In order to compensate for this offset, specially fabricated phantoms were measured prior the main imaging session.

The phantoms were prepared with agar solution 2% in which appropriate absorber was added to generate the photoacoustic signal and an agent to emit the respective fluorescence signal. India ink was used as a highly absorptive agent, whereas laser dye Sulphorhodamine B was used as a fluorescent compound with an absorption peak at 532nm when diluted in Methanol and emission range at (579-600) nm.

As presented in Figure 18, two different phantoms of random shape were tested. The upper row presents the merging of the photoacoustic and fluorescence channels before correction. Fluorescence emission is indicated with green color, whereas the respective photoacoustic signals are presented in red color. As expected, there is a slight spatial offset between these two images, which was calculated to be 4 pixels in the x axis and 5 pixels in the y axis. These values correspond to 40 μm in the x axis and 50μm in the y axis respectively.

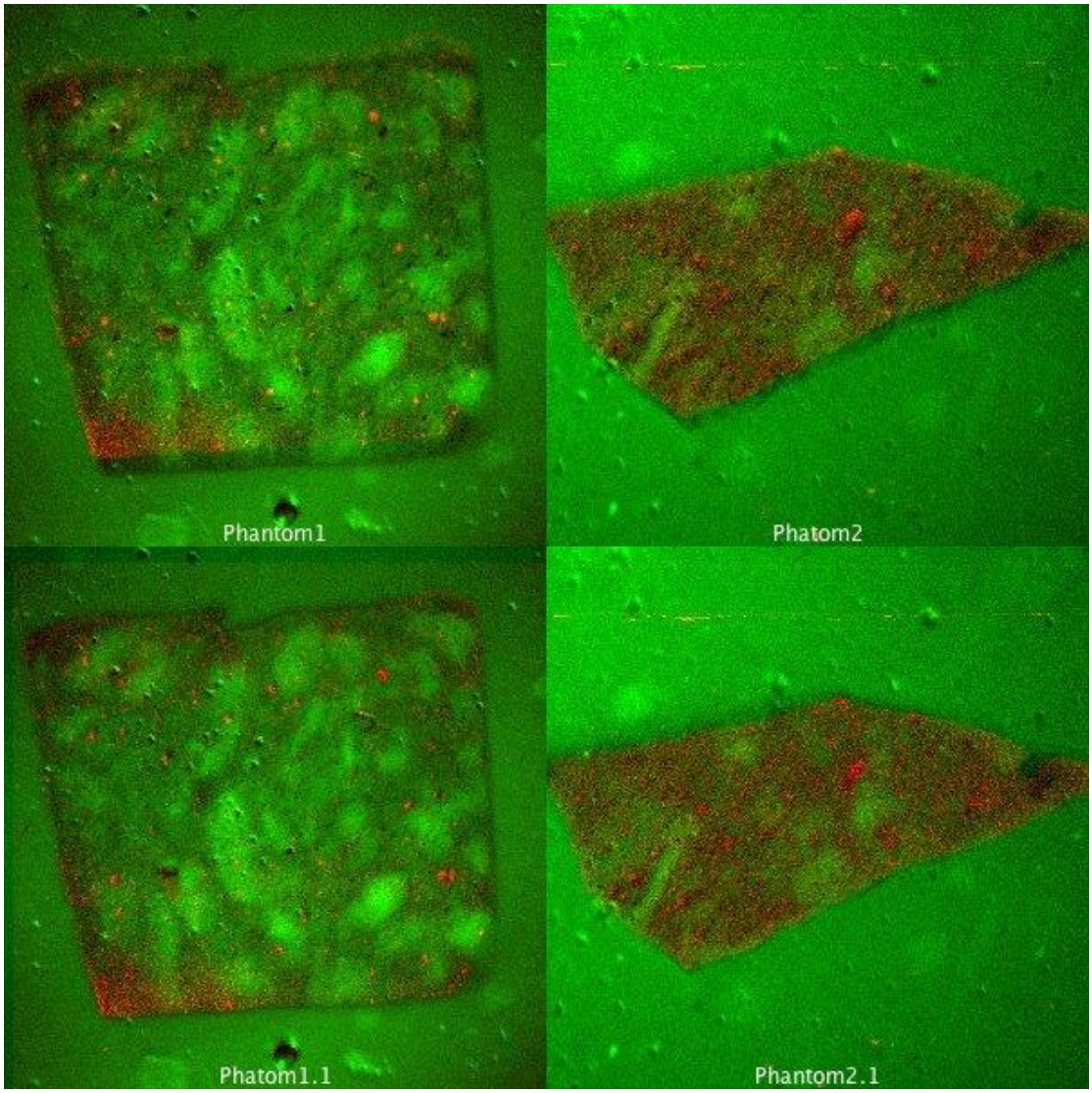

FIGURE18: RANDOM AGAR PHANTOMS CONTAINING ABSORPTION AND FLUORESCENCE AGENTS ARE SHOWN IN ORDER TO CALIBRATE THE SYSTEM BETWEEN FLUORESCENCE AND PHOTOACOUSTIC TECHNIQUE. GREEN INDICATES FLUORESCENCE SIGNAL WHILE RED THE PHOTOCOUSTICS. THE UPPER ROW SHOWS THE RESULTS PRIOR CORRECTION AND THE BOTTOM AFTER SHIFTING.

The first experiment after calibrating the system was to check if tissue samples, and more specifically the ciliary body, was able to provide autofluorescence signal. For this reason, a small part of a ciliary body was extracted and used as a sample with no further processing apart from the standard stabilization with agar. The results are presented in Figure 19 where the first autofluorescence images are shown.

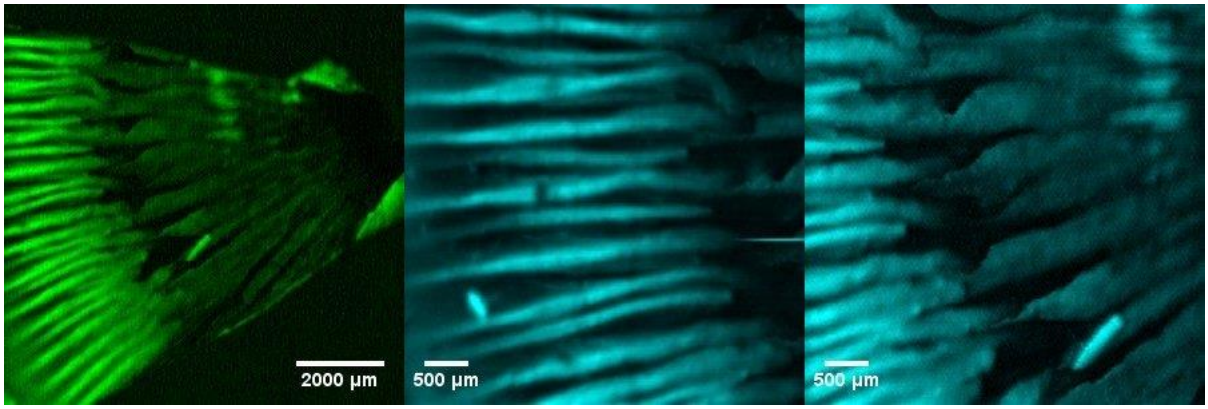

FIGURE19: FIRST AUTOFLUORESCENCE IMAGES OF A PART OF A CILIARY BODY

A part of a ciliary body is presented in the first image of Figure 19, while two subsequent zoomed in images of the same sample are further displayed. It is important to investigate whether the fluorescence and the photoacoustic signals are coregistered. As observed in Figure 20, where the same sample is measured, the two signals recorded by the two modalities seem to be different. However, since slightly different areas where scanned, the absolute merging of the images was not possible.

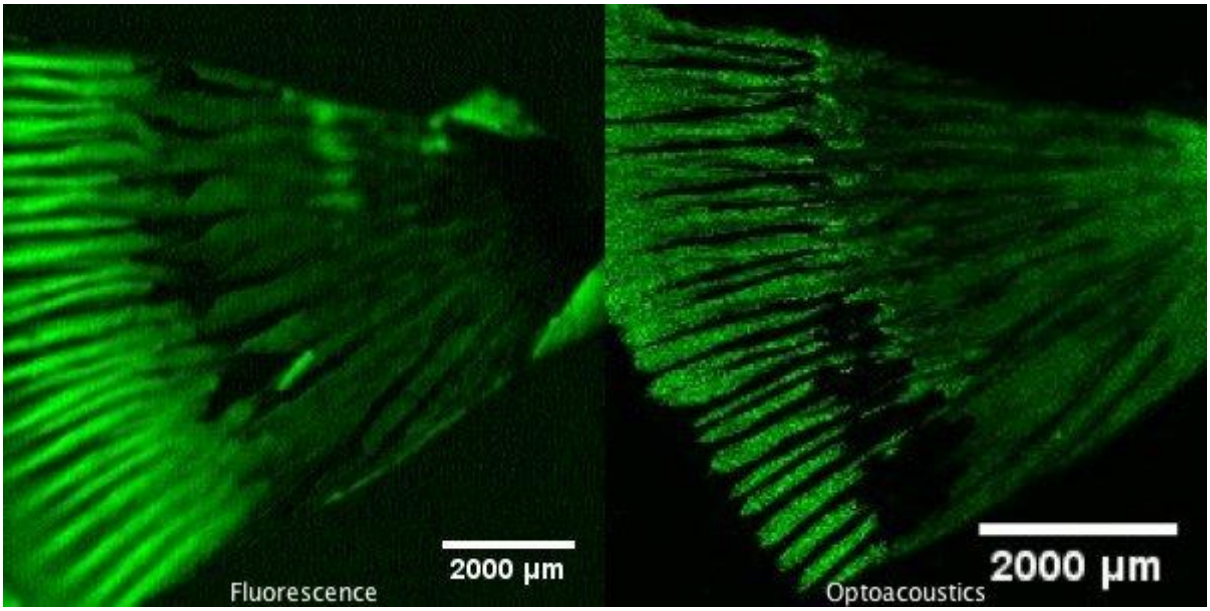

FIGURE 20: AUTOFLUORESCENCE AND PHOTOACOUSTIC SIGNAL OF THE SAME PART OF A CILIARY BODY SAMPLE.

As also presented before, a whole uncut ciliary body was tested also for autofluorescence, as shown in Figure 21. More specifically, the upper row presents the original data as obtained from the two different techniques. In the bottom row, the reconstructed photoacoustic signal is presented in depth color code, where each color indicates different slice depth. At the bottom right image, the merged autofluorescence and photoacoustic signals are shown. The area scanned was 17x17mm and the pixel size of the images is calculated to be 56.6 μm.

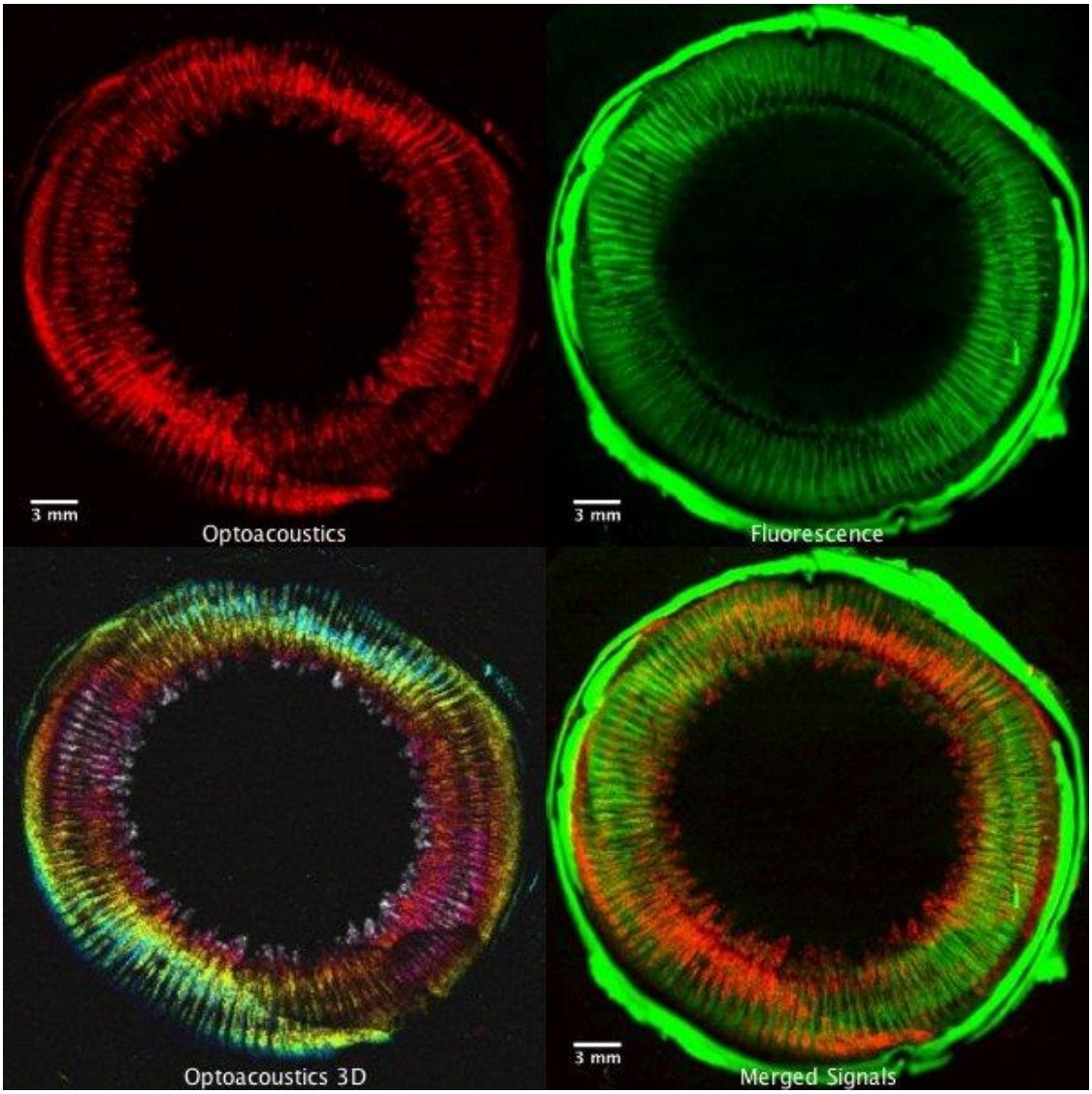

FIGURE 21: THE UPPER ROW REPRESENTS THE ORIGINAL DATA AS OBTAINED FROM THE TWO SEPARATE TECHNIQUES. THE BOTTOM LEFT IMAGE INDICATES THE RECONSTRUCTED PHOTOACOUSTIC DATA, WHERE EACH COLOR INDICATES DIFFERENT DEPTH. THE BOTTOM LEFT IMAGE IS THE MERGED SIGNALS FROM BOTH THE TECHNIQUES.

The first hypothesis made prior to the experimental procedure was that the melanin of the ciliary body would also contribute to the autofluorescence signal. However, when merging the autofluorescence and the photoacoustic data it seemed that there is an almost complementary distribution between the two signals. Therefore, it was concluded that a different molecule provides the majority of the autofluorescence signal. After a thorough bibliographic research, it was found that lipofuscin also existing in the ciliary body is the prospective molecule. In addition, to confirm these hypotheses, the experiment was reproduced with another ciliary body sample the results of which are presented below (Figure 22). The area scanned was 18x18mm with a pixel size of the image to be 60 μm.

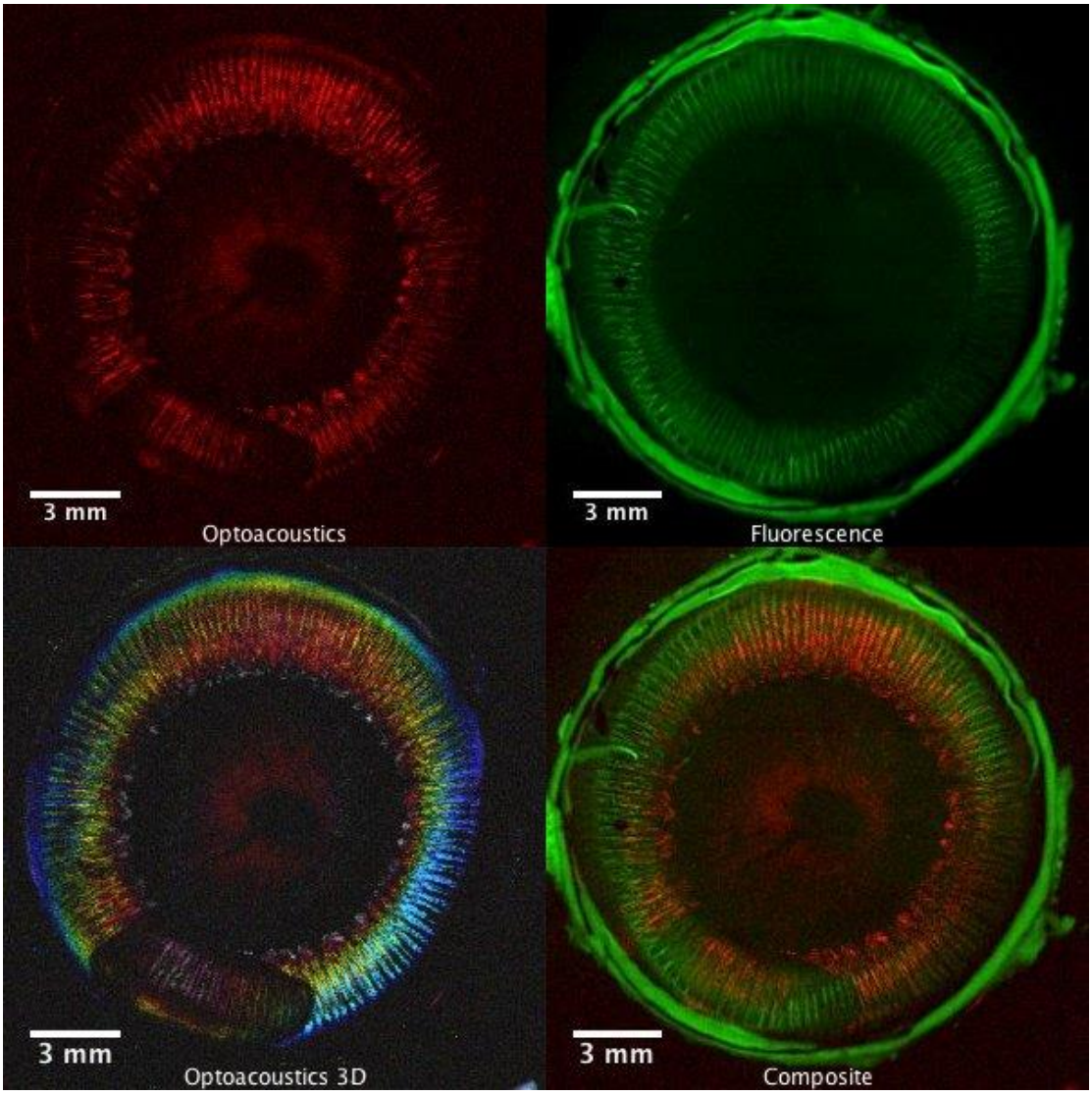

FIGURE22: THE TOP ROW SHOWS THE INITIAL DATA FROM THE TWO TECHNIQUES. THE BOTTOM LEFT IMAGE INDICATES THE DIFFERENT SLICE DEPTH OF THE PHOTOOACOUSTIC SIGNAL AND THE BOTTOM RIGHT IMAGE REPRESENTS THE COMPOSITION OF THESE TWO SIGNALS.

The second experiment confirmed the initial speculations regarding the main source of autofluorescence emission. In Figure 23 the photoacoustic signal appears slightly blurred, probably due to the fact that the sample was fixed in agar and was left in the water tank for a significant amount of time, most probably inducing increased scattering effects.

In the final study, the last uncut sample described previously, was further used for a high resolution imaging session for the observation of the ciliary ripples in greater detail. The results of this experiment are presented in Figure 23. The area scanned was 2000x2000μm and the pixel size of the respective images was 6.6 μm.

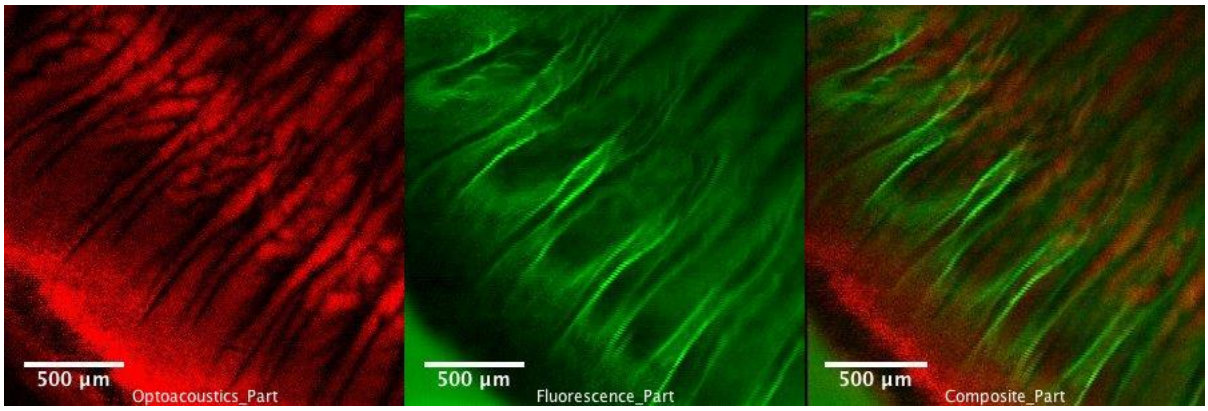

FIGURE23: ZOOMED IN AREA OF A PART OF THE PREVIOUS SAMPLE

As observed again in higher detail, there are different locations that provide signal in each case resulting in a high complementary contrast image.

F. Conclusion and Future Work

The aim of this thesis was the observation of structural features of the ciliary body of ocular models via photoacoustic imaging. The ciliary body of the eye was chosen as specimen due to the high deposition of melanin, which is considered to be an exceptional photoacoustic agent due to its intense optical absorption properties. As already mentioned, the photoacoustic effect is based on the ability of a material to absorb photons in specific wavelengths. This energy deposition causes a thermoelastic expansion of the medium and consequently a pressure difference compared to the surrounding environment. As a result, this expansion is translated into acoustic waves. The main advantage of the photoacoustic imaging technique is that it goes deeper than conventional optical microscopic modalities that are limited by light scattering, by preserving a high spatial resolution. Another great advantage of this modality is the specificity, since certain molecules absorb in certain spectral regions, therefore by choosing a set of proper wavelengths, specific absorbers can be distinguished.

The results have demonstrated the capability of the system to image not only small parts of the ciliary body with high resolution, but also uncut whole samples. In addition, by calculating the time of flight from the sample to the transducer, 3D images were obtained. In this way, the whole volume of the samples could be observed, proving that not only the ciliary body but also the iris can be imaged.

However, the combination of the two modalities was the part of the study with the major interest. Co-registration of the data of photoacoustic and autofluorescence images demonstrated that the signal originates from different areas of the ciliary body. After bibliographic research it was found that melanin is the molecule that provides the photoacoustic signal as expected, but lipofuscin is probably responsible for the majority of autofluorescence in the RPE cell layer. Previous studies are also in agreement with these findings, showing that due to the fact that the ciliary body pigmented epithelium is an extension of the RPE, it is anticipated that lipofuscin accumulates either in the pigmented epithelium or in the muscle fibers in the ciliary body.

Photoacoustic imaging has showed a rapid growth the latest years in ophthalmoscopy,

taking advantage of the fact that non-optically clear parts, or physiology of the eye (such as metabolic changes) can be structurally and functionally imaged in great detail. Furthermore, except microscopy, photoacoustic tomography (PAT) is also a promising modality that has the potential to provide more information than the conventional ocular imaging modalities, however at lower spatial resolution compared to PAM. In future research, PAT can be applied in the visualization of ocular neoplasia such as retinoblastoma and melanoma. The capability to measure microvasculature including neovascularization with high resolution is important for the diagnosis of angiogenesis. On the other hand, the RPE is also associated with several retinal diseases, including macular degeneration. In addition, in vivo studies attract large interest especially in the part of retinal and choroidal neovascularization. More related to this study, a lot of work has to be done in the future regarding quantitative imaging of the distributions of lipofuscin and melanin of the RPE in vivo, which are important for the research of clinical diagnosis of age-related macular degeneration (AMD) since the lipofuscin concentration increases with age.

The prospects of photoacoustic imaging are tremendous. By developing new systems and by optimizing several technical parameters, a rapid improvement of image quality and data acquisition speed can be achieved. Finally, the continuous innovations in laser and ultrasonic detectors technology are anticipated to promote photoacoustic imaging among the most promising modalities in order to play an indispensable role in the future of biomedical imaging and more specifically in ophthalmology.

G. References

1 Ku, G. & Wang, L. V. Deeply penetrating photoacoustic tomography in biological tissues enhanced with an optical contrast agent. *Opt Lett* **30**, 507-509 (2005).

2 Levi, J. *et al.* Molecular photoacoustic imaging of follicular thyroid carcinoma. *Clin Cancer Res* **19**, 1494-1502, doi:10.1158/1078-0432.CCR-12-3061 (2013).

3 Kim, C. *et al.* In vivo molecular photoacoustic tomography of melanomas targeted by bioconjugated gold nanocages. *ACS Nano* **4**, 4559-4564, doi:10.1021/nn100736c (2010).

4 Kitai, T. *et al.* Photoacoustic mammography: initial clinical results. *Breast Cancer* **21**, 146-153, doi:10.1007/s12282-012-0363-0 (2014).

5 Hu, S., Rao, B., Maslov, K. & Wang, L. V. Label-free photoacoustic ophthalmic angiography. *Opt Lett* **35**, 1-3, doi:10.1364/OL.35.000001 (2010).

6 Wang, X. *et al.* Noninvasive laser-induced photoacoustic tomography for structural and functional in vivo imaging of the brain. *Nat Biotechnol* **21**, 803-806, doi:10.1038/nbt839 (2003).

7 Maslov, K. & Wang, L. V. Photoacoustic imaging of biological tissue with intensity-modulated continuous-wave laser. *J Biomed Opt* **13**, 024006, doi:10.1117/1.2904965 (2008).

8 Hu, S. & Wang, L. V. Neurovascular photoacoustic tomography. *Front Neuroenergetics* **2**, 10, doi:10.3389/fnene.2010.00010 (2010).

9 Huang, D. *et al.* Optical coherence tomography. *Science* **254**, 1178-1181 (1991).

10 Greenberg, J. P. *et al.* Quantitative fundus autofluorescence in healthy eyes. *Invest Ophthalmol Vis Sci* **54**, 5684-5693, doi:10.1167/iovs.13-12445 (2013).

11 Rao, B., Li, L., Maslov, K. & Wang, L. Hybrid-scanning optical-resolution photoacoustic microscopy for in vivo vasculature imaging. *Opt Lett* **35**, 1521-1523, doi:10.1364/OL.35.001521 (2010).

12 Jiang, M., Zhang, X., Puliafito, C. A., Zhang, H. F. & Jiao, S. Adaptive optics photoacoustic microscopy. *Opt Express* **18**, 21770-21776, doi:10.1364/OE.18.021770 (2010).

13 Zhang, X., Zhang, H. F. & Jiao, S. Optical coherence photoacoustic microscopy: accomplishing optical coherence tomography and photoacoustic microscopy with a single light source. *J Biomed Opt* **17**, 030502, doi:10.1117/1.JBO.17.3.030502 (2012).

14 Zhang, X., Zhang, H. F., Puliafito, C. A. & Jiao, S. Simultaneous in vivo imaging of melanin and lipofuscin in the retina with photoacoustic ophthalmoscopy and autofluorescence imaging. *J Biomed Opt* **16**, 080504, doi:10.1117/1.3606569 (2011).

15 Wang, L. V. & Wu, H.-I. *Biomedical optics : principles and imaging*. (Wiley, 2007).

16 Li, C. & Wang, L. V. Photoacoustic tomography and sensing in biomedicine. *Physics in medicine and biology* **54**, R59-97, doi:10.1088/0031-9155/54/19/R01 (2009).

17 Lorenzo, J. R. & ebrary Inc. xvii, 336 p. (World Scientific Pub. Co.,, Singapore, 2012).

18 Ntziachristos, V. Going deeper than microscopy: the optical imaging frontier in biology. *Nat Methods* **7**, 603-614, doi:10.1038/nmeth.1483 (2010).

19 Yao, J. & Wang, L. V. Photoacoustic Microscopy. *Laser Photon Rev* **7**, doi:10.1002/lpor.201200060 (2013).

20 Peate, I. & Nair, M. *Fundamentals of anatomy and physiology for nursing and healthcare students*. Second edition. edn.

21 Delamere, N. A. Ciliary Body and Ciliary Epithelium. *Adv Organ Biol* **10**, 127-148, doi:10.1016/S1569-2590(05)10005-6 (2005).

22 Tserevelakis, G. J., Tsagkaraki, M. & Zacharakis, G. Hybrid photoacoustic and optical imaging of pigments in vegetative tissues. *J Microsc* **263**, 300-306, doi:10.1111/jmi.12396 (2016).

23 Tserevelakis, G. J., Soliman, D., Omar, M. & Ntziachristos, V. Hybrid multiphoton and optoacoustic microscope. *Opt Lett* **39**, 1819-1822, doi:10.1364/OL.39.001819 (2014).

H. Acknowledgements

This current thesis was accomplished in the In Vivo Imaging Lab (IVIL) of the Institute of Electronic Structure and Laser (IESL) of FORTH and in context of the fullfilment of my Master Thesis at the interdeartemental programm of “Optics and Vision” of the Faculty of Medicine. Since this work signifies the end of an important period, and it is a result of personal but mainly collective work, I would like to thank the people below.

Firstly, Prof. Miltiadis Tsilimbaris for giving me the chance of fulfilling this thesis, for his attention and critical guidance throughout this year and for introducing me to the world of opthalmoscopy, that has proven to be of great interest.

Furthermore, I would like to thank Dr. Giannis Zacharakis for providing me the opportunity to work in IVIL lab for few more years and offering me additional perspectives in my research interest. I strongly appreciate him for being there as a great mentor and a good friend.

Most of all, I want to thank Dr. George Tserevelakis for not only developing the imaging set up, without which none of this work would have been done, but mainly for letting me get accustomed in the new world of photoacoustics and opening new possiblilities for me. He was the one suppervising me through every step and a person to count on every difficulty. I thank him as a collegue and a new friend, making also working hours pleasant.

Of course I want to thank every new and old member of the IVIL lab as well as the colleques from the office for being supportive when necessary, for exchanging new ideas and for making days delightful.

Finally, great gratitude to my family and friends for supporting and trsusting in me through this time. They made even the worst days, happy.